Evaluating the Behaviour of Functionally Graded Reinforced Concrete without Transverse Reinforcement using Distributed Sensing

Jacob Yager[a], Neil A Hoult[b], and Evan Bentz[c]

[a] Department of Civil Engineering, Queen's University, 58 University Ave., Kingston, On. Canada, K7L 3N6, 15jy36@queensu.ca (corresponding author)

[b] Department of Civil Engineering, Queen's University, 58 University Ave., Kingston, On. Canada, K7L 3N6, neil.hoult@queensu.ca

[c] Department of Civil & Mineral Engineering, University of Toronto, 35 St. George St., Toronto, On., Canada, M5S 1A4, bentz@ecf.utoronto.ca

The following material is an accepted manuscript. The link to the formal publication can be found below:

https://www.sciencedirect.com/science/article/pii/S0950061821013726

Abstract

Functionally graded concrete (FGC) can lower cement content and CO_2 emissions. However, the behaviour of FGC is not fully understood. To examine behaviour at concrete interfaces as well as global behaviour, horizontally and vertically layered FGC (HLFGC, VLFGC) and control beams, all without transverse reinforcement, were tested in three-point bending. Distributed sensing measured reinforcement strains, cracking behaviour, and load-deflection behaviour. Using fibre reinforced concrete increased the load carrying capacity of VLFGC and decreased the number of cracks and the cracking load for HLFGC. Cracking at interfaces produced lower cracking strengths in VLFGC beams and brittle failures in some HLFGC beams.

Keywords

Functionally graded concrete; distributed fibre optic strain sensing; digital image correlation; three-point bending tests; debonding; low cement concrete; fresh on fresh concrete casting; fibre reinforced concrete

1.0 Introduction

The production of cement is responsible for 5-7% of global CO_2 emissions [1], and concrete is the most used building material in the world [2]. To reduce these CO_2 emissions, and the associated climate change impact, potential solutions include lowering the use of cement, modifying the production of cement, designing more efficient structures, and producing less construction waste. One such strategy for reducing cement usage is the use functionally graded concrete [3].

Functionally graded concrete (FGC) is comprised of multiple strategically placed concrete mixes in one or more dimensions of a concrete element to increase performance while saving material or weight [3]. By optimizing the cement use for the localized functional requirements along an element, the design needs can be efficiently met while reducing cement use and, thus, CO_2 emissions.

Despite the potential environmental benefits of using FGC, limited research has been undertaken on the behaviour of functionally graded reinforced concrete elements. Potential issues might develop in locations of changes in stiffness within the element, where there is a transition from one concrete type to another, causing localized increases in reinforcement stresses and crack widths. Conventional sensing technologies such as strain gauges, however, often do not measure the critical strain due to a lack of a priori knowledge about where cracks and stress concentrations will develop [4]. Distributed measurement technologies provide a method of capturing potential localized effects that result from the use of FGC. To investigate the behaviour of FGC and its concrete interfaces, digital image correlation (DIC) and fibre optic sensors (FOS) are employed in this investigation. DIC is the process of tracking surface deformations using a camera and can be used to capture crack widths and crack patterns [5,6]. FOS can be used to provide distributed strain measurements along the length of a rebar and have been used to examine the behaviour of reinforced concrete (RC) beams [4,7-10]. Although neither technique has yet been used to characterize the behaviour of FGC, the use of DIC and FOS on FGC may provide a better understanding of the behaviour of FGC specimens as well as enable the quantification of issues that arise, such as cracking at concrete interfaces. Thus, in the current research, a series of specimens with nominally identical geometry and reinforcing, but with three different concrete mixes (i.e. a low strength / low cement mix, a normal strength / normal cement mix, and a high strength / high performance mix) and either horizontal or vertical grading will be tested to assess the behaviour of FGC elements using distributed sensing.

The objectives of this research are to: (i) determine the impact of mix type, interface quality, and functional grading on deflection behaviour, (ii) evaluate distributed longitudinal reinforcement strains in FGC to measure and characterize reinforcement stress concentrations due to grading, (iii) assess the cracking behaviour of FGC, specifically locating and measuring cracks in graded specimens, and (iv) identify and quantify problems associated with interfaces in FGC.

2.0 Background

2.1 Functionally Graded Concrete

FGC was originally conceived for applications that focused on durability and crack control [11-15]. Maalej et al. [12] compared the corrosion performance of horizontally layered FGC (HLFGC) with a bottom layer of ductile fibre reinforced cementitious composite and a top layer of ordinary concrete to that of a uniform ordinary concrete beam. Both types of beams were exposed to accelerated corrosion, but the HLFGC beam took 70% longer to reach the same level of corrosion as the uniform beam, as well as lacking any corrosion induced cracking.

In addition to corrosion protection, crack performance has been found to be improved using FGC. Fracture energy increased with the introduction of a horizontal layer of fibre reinforced concrete (FRC) [13-14]. In addition, crack widths were decreased using HLFGC with FRC [11,15]. Li and Xu [15] utilized ultrahigh toughness cementitious composite (UHTCC) in HLFGC to reduce cracking and increase flexural capacity in concrete beams without transverse reinforcement. A layer of UHTCC of varying heights was overlaid by ordinary concrete and the HLFGC beams were tested in four-point bending. It was determined that a 35 mm (just above reinforcement level) layer of UHTCC provided the optimum performance in terms of durability versus cost. The UHTCC provided not only a decrease in crack widths to less than or equal to 0.05 mm before yielding but also a 30% increase in load carrying capacity and 70% increase in the ductility index compared to an ordinary RC beam. In addition to durability and crack performance, unreinforced FGC designed with a layer of steel FRC, has been shown to increase flexural capacity compared to ordinary unreinforced concrete beams or slabs. While not directly comparable to beams with tensile reinforcement since the presence of reinforcement will decrease the impact of fibres on strength, the strength increases due to the use of fibres is noteworthy. Up to 15 times flexural strength increases for double layers of 3% steel fibres in RC beams without reinforcement [16], 5 times flexural strength increases for unreinforced beams with a 3% steel fibre layer [17], and 2.5 times flexural strength increases for unreinforced slabs with a 2% steel fibre layer [18] have been found. Extensive tests have also been performed on non-FGC RC beams without transverse reinforcement. A series of tests completed by Kuchma and Collins [19] included many beams without transverse reinforcement, including some similar in size to those tested in this experimental program.

FGC has also been used for cement, material, and weight savings [20-26]. Herrmann and Sobek [20] combined the traditional HLFGC design with vertically layered FGC (VLFGC) for weight savings in concrete beams without transverse reinforcement. Low porosity (high density) concrete layers on the top and bottom of the beam sandwiched a middle layer that consisted of 3 sections. The outer thirds of this middle section consisted of medium porosity (medium density) concrete, while the centre third was a layer of high porosity (low density) concrete. While still achieving minimum strength requirements, a 43% weight reduction was achieved. Other research has achieved weight savings of 42% using fibre reinforced lightweight concrete in HLFGC [21], and embodied carbon and cost reductions of 37.7% and 81.1% were achieved using recycled aggregate concrete HLFGC [22]. Cement savings of 25% and weight savings of 30% were achieved using a U-shaped FGC specimen [23], and 10% cement reductions were achieved with the use of fly ash in HLFGC [24]. While the previous research has identified the potential weight and cement savings, serviceability issues such as premature cracking at layer interfaces and associated strain concentrations in reinforcement exist. However, these issues have not been fully understood and investigated through the use of distributed sensing.

While FGC has many benefits in terms of material savings, crack control and durability, and ultimate capacity, challenges in pouring FGC exist. The main issue occurs with the interface between the two types of concrete. This may be less of an issue with continuously graded FGC, where pronounced boundaries do not exist. Therefore, the future in FGC may be in continuous gradation through the use of robotics and automated construction [20]. However, this technology is not yet ready for use so layered production is an often-used method used for pouring FGC. Pouring of layered FGC can be done using either fresh on hardened concrete casting or fresh on fresh concrete casting [3]. Fresh on hardened concrete casting, which pours fresh concrete on already cured concrete, is not optimal for FGC due to the slow production speed, extra reinforcement required between layers, and differential shrinkage. However, fresh on hardened casting is extensively used for various applications in the precast industry for connections or the creation of composites. Advantages include assuring the geometry of the layering can be accurately monitored, only requiring one mix to be used at one time, and the existence of codified methods to assess the bond strength of cold joints [3]. Fresh on fresh concrete casting may be more promising for FGC due to its reduced production times, good bond between the two layers without transverse reinforcement, and more limited strain incompatibilities compared to fresh on hardened casting. Nevertheless, limited research on this production technique exists, and problems such as mix compatibility, resulting in cracking at interfaces, and concrete flow between the two interfaces may occur [3]. In the current study, specimens with multiple levels of mix integration at the fresh on fresh cast interfaces will be tested to investigate the impact on serviceability and element performance.

2.2 Distributed Fibre Optic Sensing

Distributed FOS can be used to measure longitudinal strain along a reinforcement bar. FOS, as opposed to more conventional strain gauges, are corrosion resistant, can provide distributed measurements, are not affected by electromagnetic interference, are relatively small, and the sensing cables can be inexpensive (~$0.15/m). In this study, a Rayleigh backscatter distributed FOS system is employed, which is more suitable when smaller sensing ranges with higher accuracy are needed [10].

Rayleigh backscatter FOS have been used extensively to measure longitudinal reinforcement strains in RC. Regier and Hoult [7] used distributed FOS to detect localized deterioration in reinforcement bars. Davis et al. [8] resolved issues with cracking and local bending in the reinforcement by using a coating around the fibre and instrumenting both sides of the bar. Barrias et al. [9] were able to use polyimide coated FOS embedded in a reinforcement bar to measure strain reliably up until a load that resulted in significant stiffness changes and damage to rebar. Brault and Hoult [4] determined the optimum installation technique for FOS on reinforcement was to use nylon coated single-mode fibre bonded with cyanoacrylate and protected with silicone. This method provided the most accurate measurements compared with discrete strain gauge measurements. Poldon et al. [10] correlated strain peak measurements to crack widths using FOS and DIC in a large RC beam. However, none of these studies investigated the implications of having interfaces between different concretes within a specimen.

3.0 Experimental Procedure

3.1 Specimens

Nine different RC beam types, as seen in Figure 1, were fabricated. The beams had an overall length of 1200 mm, height of 150 mm, effective depth of 115 mm, and width of 100 mm. Each beam contained 1-10M deformed rebar (A_s = 100 mm^2), which had a yield strength of 584 MPa. The weldable grade rebar meets the CSA G30.18 standard [27]. The straight bar anchorage was designed according to CSA A23.3 to ensure adequate development length. A clear cover at the ends of the rebar of 20 mm was used. It should be noted that due to the small member size and use of a single rebar in these beams, it was hypothesized that some variability in load deflection behaviour, reinforcement strain behaviour, and cracking behaviour was expected. Three concrete types were used: low strength/low cement concrete (referred to as LS), normal strength/normal cement concrete (referred to as NS), and high strength fibre reinforced concrete (HSFRC) with polypropylene (PP) fibres and normal cement content (referred to as HF). SikaFiber Force 600 macro synthetic structural fibres were used, which, according to the product data sheet, have a tensile strength of 448 MPa, elastic modulus of 4 GPa and a length of 50 mm [28]. The fibres had a measured width of 2 mm. Compressive strengths and age at testing for the cylinder tests and beam tests can be seen in Table 1. The statistical analysis for the cylinder tests can be seen in Table 2. The mix design for each of the mixes can be seen in Table 3. The maximum specified coarse aggregate size in the concrete mixes was 14 mm and the cement used was high early strength cement. ViscoCrete 2110, a high range water reducing admixture and superplasticizer, was used in the HF mix. Three uniform beams, which serve as the controls (one for each of the three concrete types used), and six types of FGC beams (three horizontally layered and three vertically layered) were constructed. Three duplicate beams were made to examine the effects of different interface and compaction qualities. One horizontally layered FGC (HLFGC) beam and two vertically layered FGC (VLFGC) beams were remade, making the total number of specimens tested 12. The three control beams were called LSC-1, indicating it was the low strength control (top left in Figure 1), NSC-1, indicating the normal strength control (middle left), and HFC-1, indicating the high strength fibre reinforced control (bottom left).

The HLFGC beams were designed to explore the influence of having a layer with increased tensile strength on cracking and strain behaviour. These specimens had low strength concrete on the top and a layer of HSFRC on the bottom where the specimen name indicates the thickness of the HSFRC layer. The HLFGC beams were H20 (top right in Figure 1), H35 (middle right), and H50 (bottom right). The HLFGC specimens were poured such that the bottom layer of HSFRC reached the desired height, then vibrated with a poker vibrator that was inserted periodically along the length of the beam for about 10 seconds per location, and then the low strength concrete was poured on top of the bottom layer and vibrated in the same way. The pouring of the two layers was done within 30 minutes of each other to allow minimal curing of the first layer before the second layer was poured.

The VLFGC beams were designed to investigate the impact of a vertical interface within a section on the global beam behaviour as well as the local strain in the reinforcement and cracking at the interface between concrete types. The VLFGC beam names indicate the arrangement of the concrete types of the vertical layers. For example, specimen LNL indicates that the beam had low strength concrete (L) on the sides and normal strength concrete (N) in the centre. The VLFGC beams were LNL (top centre in Figure 1), LHL (middle centre), and NHN (bottom centre). The VLFGC specimens were constructed with 2 mm thick wooden dividers placed in between the concrete types during pouring of the concrete. Each layer was vibrated individually with a poker vibrator inserted into the center of each region for approximately 10 seconds. The dividers were then removed, and the concretes were then vibrated again in the same way to close the interface gap.

Three beams (LNL, NHN, and H35) were produced twice to examine the effects of the level of compaction and interface gap closure. For LNL-1 and NHN-1 after removal of the section dividers, the outside of the formwork was vibrated with a poker vibrator at the midpoint of each individual concrete section for approximately 10 seconds each. Both the high strength and low strength mixes were also stiffer when wet than the normal strength mix. The lack of vibrating at the interface and the high stiffness of two of the mixes resulted in improper closure of the gap between the two concrete sections. For LNL-2 and NHN-2, the high and low strength mixes were more workable, and the poker vibrator was used to vibrate the outside of the forms for approximately 10 seconds at each interface location instead of only at the centre of the individual regions. These changes ensured the gap between the sections were closed. Similarly, for specimen H35-1, only one side of the outside of the forms was vibrated, which resulted in significant voids developing at the interface between layers on one side of the beam, whereas for H35-2 the poker vibrator was used to vibrate both sides of the beam eliminating the visible voids between the layers.

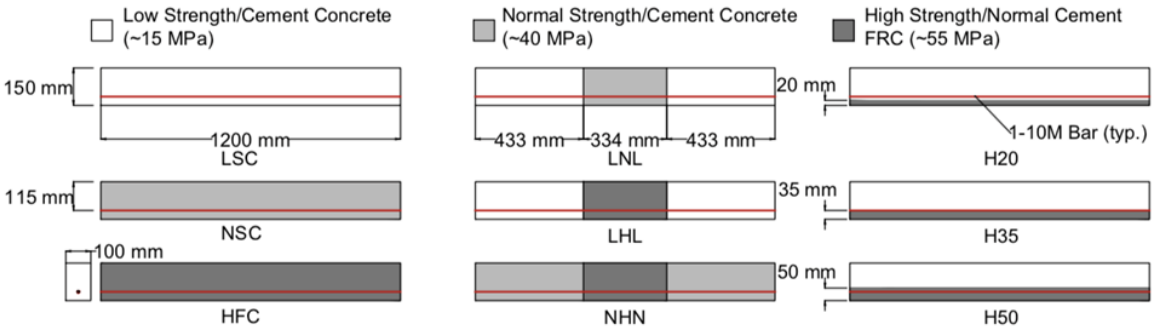

Figure 1. Specimen geometry and types

Table 1. Concrete compressive strengths and age at testing

Specimen	Age at beam test (days)	Concrete type	Age at cylinder test (days)	Compressive strength (MPa)	Concrete type	Age at cylinder test (days)	Compressive strength (MPa)
LSC-1	42	LS-1	34	16	-	-	-
NSC-1	40	NS-1	34	41	-	-	-
HFC-1	41	HF-1	34	59	-	-	-
LNL-1	32	LS-1	34	16	NS-1	34	41
LHL-1	45	LS-1	34	16	HF-1	34	59
NHN-1	46	NS-1	34	41	HF-1	34	59
H20-1	42	LS-2	42	16	HF-2	42	51
H35-1	33	LS-1	34	16	HF-1	34	59
H50-1	47	LS-1	34	16	HF-1	34	59
LNL-2	41	LS-2	42	16	NS-2	41	34
NHN-2	42	NS-2	41	34	HF-2	42	51
H35-2	41	LS-2	42	16	HF-2	42	51

Table 2. Statistical analysis of concrete cylinder compressive strength tests

Concrete Type	Average (MPa)	Number of Samples	St. Dv. (MPa)	COV
HF-1	59.1	4	5.0	8.4%
HF-2	50.5	4	5.4	10.6%
NS-1	40.7	3	3.8	9.3%
NS-2	34.5	2	0.2	0.4%
LS-1	16.4	4	2.4	14.6%
LS-2	15.6	4	1.1	7.4%

Table 3. Concrete mix design

	LSC density (kg/m3)	NSC density (kg/m3)	HFC density (kg/m3)
water	150	215	145
cement	230	474	430
coarse aggregate	800	1000	1080
fine aggregate	1200	505.3	835
superplasticizer	-	-	2.5
polypropylene fibres	-	-	5
w/cm	0.65	0.45	0.34

3.2 Instrumentation

Each of the beams were instrumented with Linear Potentiometers (LP), FOS, and a digital camera to capture images for DIC analysis. The entire set up can be seen in Figure 2(a), while a schematic of the beam test setup can be seen in Figure 2(b).

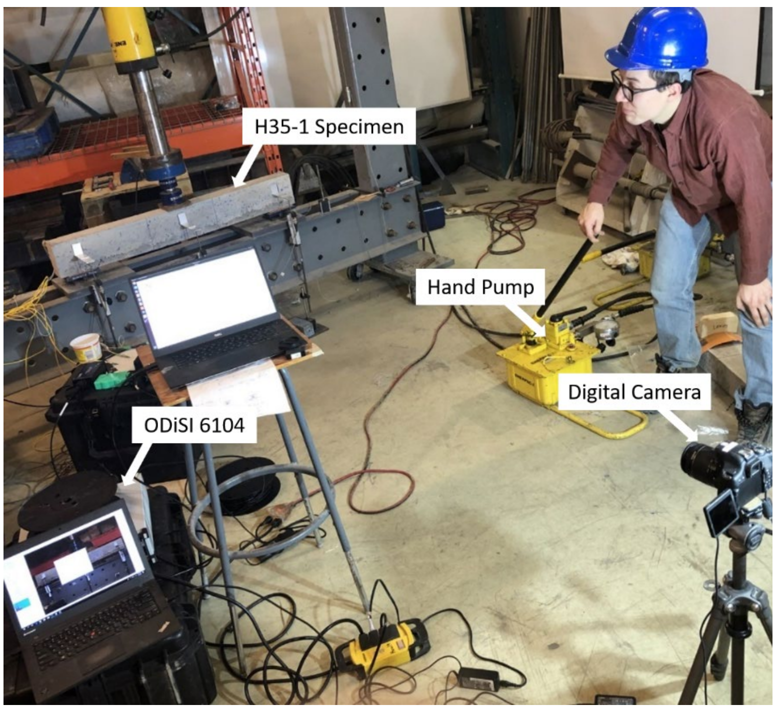

(a) Specimen and instrumentation

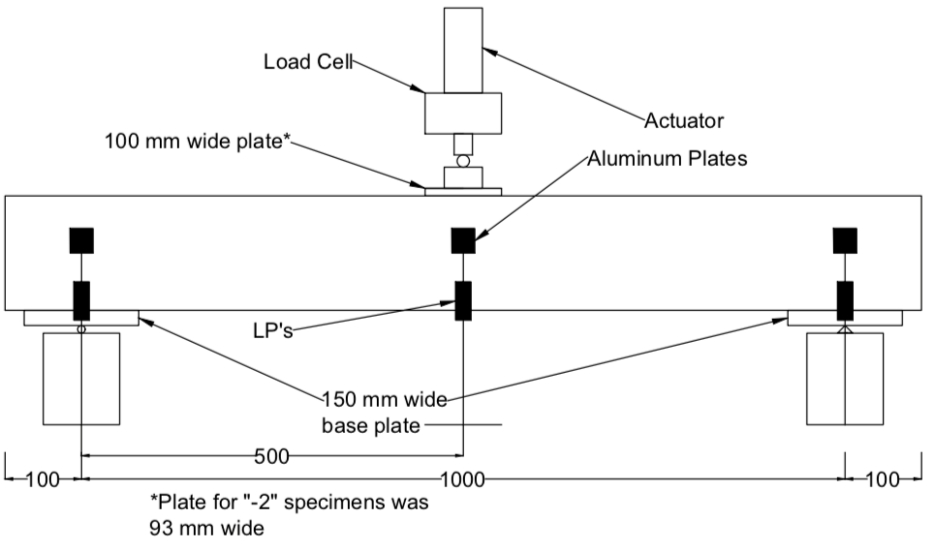

(b) Schematic of test setup (all dimensions in mm)

Figure 2. Beam test setup

Nylon coated fibre optic cables were bonded to both sides of the 10M rebar in each beam. The procedure outlined by Brault and Hoult [4] was used, which consisted of first grinding and sanding the reinforcement along the path where the nylon-coated fibre optic cable would be installed. After sanding, the path was cleaned with degreaser, water, and then 99% isopropyl alcohol. The nylon fibre was glued down with cyanoacrylate adhesive. PVC tubing was taped down to 25 mm of the rebar at both ends of the rebar on both sides, and the fibre was fed through the tubing to protect the fibre that was not bonded to the bar inside the formwork during the concrete pour. Lastly, after the glue dried, silicone was applied on top of the fibre to further protect the fibre from the concrete.

To obtain surface crack widths and crack patterns, a Canon EOS Rebel T6i digital camera was placed approximately 2 m away from the beam to take pictures, as seen in Figure 2(a). The beam was spray painted with black or blue dots to make a speckle pattern to be used in conjunction with DIC analysis using GeoPIV-RG with a patch size of 64 pixels.

To obtain deflection data, linear potentiometers (LPs), with a stroke of 100 mm and an accuracy of 0.1 mm, were placed at midspan and the supports of the beam. Three L-shaped aluminum plates were glued to the beam with an epoxy at mid-height over each of the supports and at mid span, as seen in Figure 2(b). The LPs were placed underneath the overhanging aluminum plate, which deflected with the beam. To calculate the total deflection, the average deflection at the supports was subtracted from the deflection at midspan. The load was measured using a 300 kN load cell mounted between the actuator and the beam.

3.3 Testing Procedure

The beams were tested in three-point bending using a hand pump. The load was applied at a rate of approximately 0.14 kN/s. As seen in Figure 2(b), the supports were placed at 100 mm away from the ends of the beam, for a tested span of 1000 mm. Base plates with a width of 150 mm were placed at the supports, and a 100 mm wide plate was placed under the load cell as seen in Figure 2(b). The support at the left end was a roller, while the support on the right end was a captive roller. A Luna Technologies

ODiSI 6104 was used to measure and record the FOS data at a rate of 2 Hz. The accuracy of this system is 25-30 microstrain, with a gauge length of as low as 0.65 mm and a sensing range of up to 50 m [29]. Pictures were taken at 0.5 Hz, while the load cell and LP measurements were recorded at 2 Hz.

4.0 Results

4.1 Load Deflection Behaviour

Figure 3 and 4 display the load deflection behaviour of all the beams tested. Figure 3(a) shows the complete load-deflection response for each of the control beams, Figure 3(b) shows the VLFGC beams along with the normal strength control (NSC-1), and Figure 3(c) shows the HLFGC beams along with NSC-1. The saw tooth pattern seen in the figures was a result of the hand pump load application, as relaxation occurred as the pump handle was lifted during pumping. HFC-1 exhibited the highest load carrying capacity of 29.3 kN due to the higher compressive strength of the concrete and the influence of PP fibres, and it demonstrated ductility after yield reaching a total deflection of 43 mm, also potentially due to the presence of the fibres. NSC-1 and LSC-1 achieved peak loads of 25.5 and 25.2 kN, respectively, and experienced ductile failures, with LSC-1 reaching over 60 mm of deflection, at which point, the test was stopped.

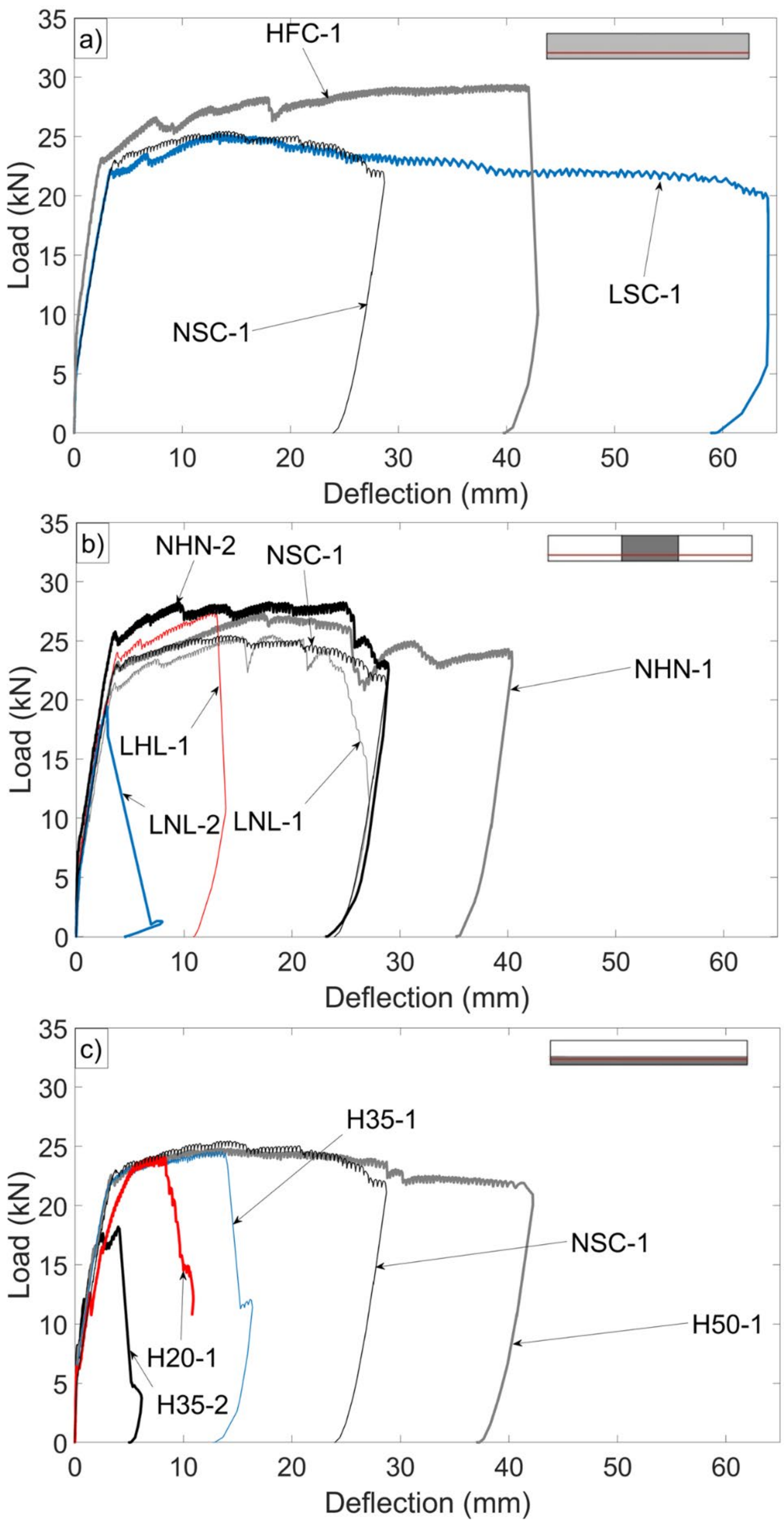

Figure 3. Load-deflection behaviour (complete test): (a) Control beams, (b) VLFGC and NSC-1 beams, (c) HLFGC and NSC-1 beams

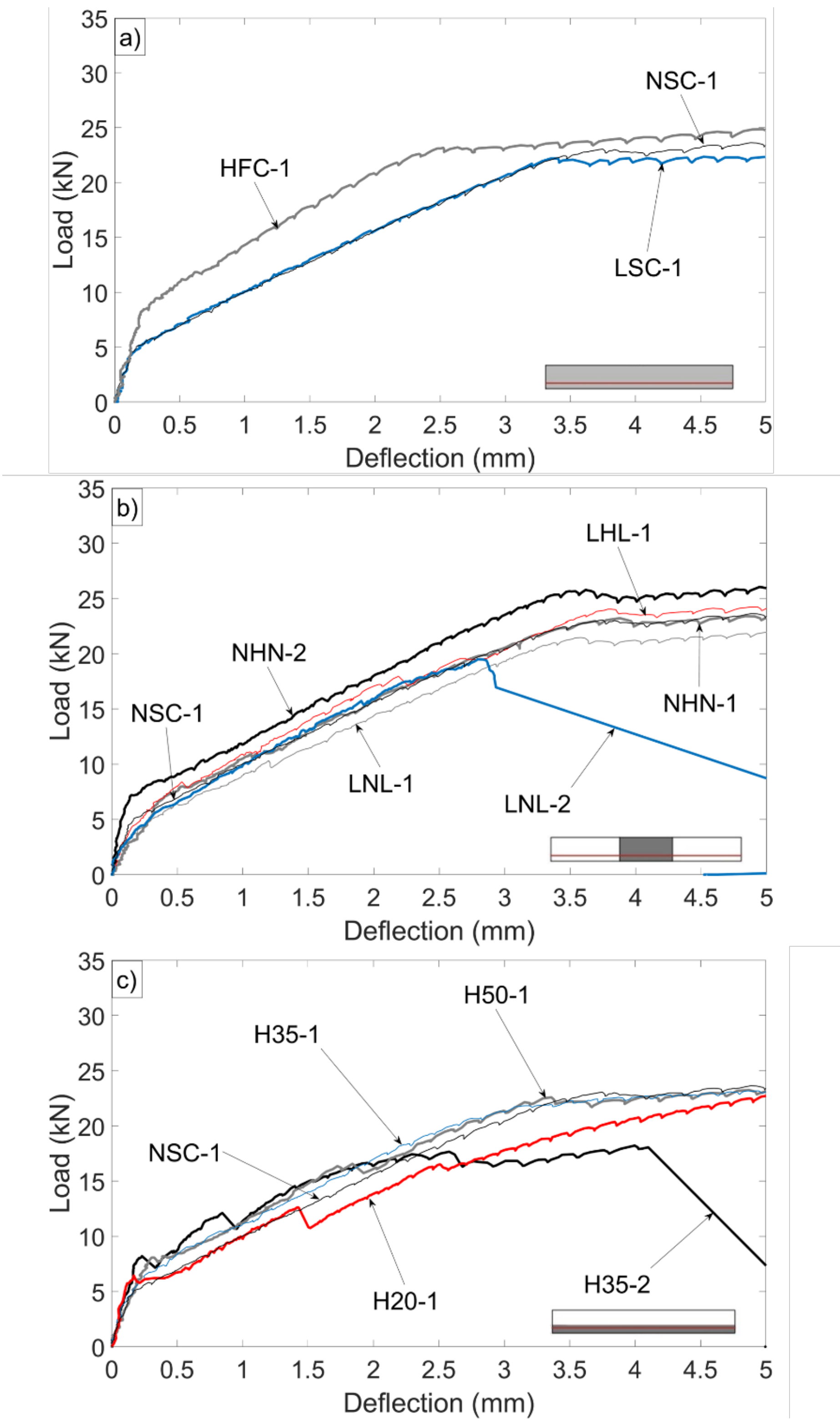

Figure 4. Load-deflection behaviour (pre-yield): (a) Control beams, (b) VLFGC and NSC-1 beams, (c) HLFGC and NSC-1 beams

The VLFGC beams with high strength concrete in the midspan region (LHL-1, NHN-1, and NHN-2) also saw increases in load carrying capacity compared to NSC-1 and achieved peak loads of 27.5, 27.3, and 28.2 kN, respectively, as tensile fibres may have provided additional tensile capacity for these beams. Specimen LNL-1 had a load carrying capacity comparable to the NSC-1 and LSC-1. However, LNL-2, despite having no visible gap at the interface (see Figure 5), experienced a brittle shear failure pre-yield at 19.5 kN. This difference between the LNL specimens highlighted the variability that exists in these beams and it is hypothesized that this may be due to the small size of the beams and the use of only one reinforcing bar. LHL-1 and LNL-2 both experienced brittle shear failures with deflections at failure of 13 mm and 3 mm, respectively. NHN-1 and NHN-2, on the other hand, experienced ductile failures at deflections higher than 25 mm. The lower strength concretes in the outer regions were potentially more susceptible to brittle shear failures since lower strength concretes are weaker in shear [30].

For the HLFGC beams, the peak loads for H20-1, H35-1, and H50-1 were 24.2, 24.6, and 24.8 kN, respectively, which were similar to NSC-1. However, H35-2 failed pre-yield at a load of 18.2 kN. This again demonstrated the variability of beams of this size. Additionally, all HLFGC beams, besides the H50-1 specimen, saw brittle shear failures or concrete interface bond failures as indicated by the sudden reduction in load carrying capacity in Figure 3(c) and the failure images in Figure 6. The issues surrounding beams with horizontal interfaces at or below reinforcement level will be discussed further in later sections but was also observed at the rebar level by Li and Xu [15].

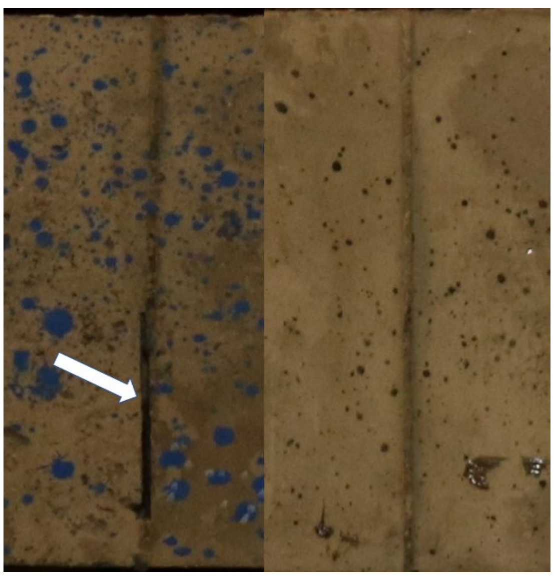

Figure 5. Gap at interface prior to loading of LNL-1 (left) vs LNL-2 (right)

Figure 4 displays the load deflection behaviour for the first 5 mm of deflection for all specimens. Figure 4(a) presents the control beams, Figure 4(b) the VLFGC beams, and Figure 4(c) the HLFGC beams. The introduction of the HSFRC influenced the cracking load as HFC-1 had the highest cracking load at about 8 kN, while the HLFGC beams had cracking loads of about 6 kN, and the other control beams had cracking loads below 5 kN. For the VLFGC beams (besides NHN-2), cracking started below 5 kN with cracking at the interface starting at loads as low as 3.1 kN in NHN-1. NHN-2, which did not have a gap at the interface, did not crack until about 7 kN, and this crack was not an interface crack. The difference between a visible gap and a non-visible gap is shown in Figure 5, with LNL-1 having a visible gap indicated with an arrow. Thus, it was possible to fabricate a VLFGC beam that cracked at loads higher than the normal concrete control. However, LNL-2, which also had no visible gap at the interface, did crack first at the interface at a load of 5 kN. The increase in the cracking load for the HFC-1 and the HLFGC specimens was expected due to the presence of fibres, which have been seen to increase fracture energy, thus increasing the cracking load [13-14]. Likewise, the introduction of HSFRC increased the stiffness of HFC-1 and led to slight increases in the stiffness of the HLFGC specimens compared to the NSC-1 and LSC-1. The VLFGC specimens (besides NHN-2) had lower stiffnesses since cracking started at a load at or below 5 kN at the interfaces. Drops in the load deflection curve, such as the one seen on the H50-1 curve at a 1.8 mm deflection, H20-1 at 1.5 mm, and H35-2 at 0.8 mm among others, were due to the formation of cracks, which was confirmed with fibre optic strain data.

LSC-1 Concrete crushing (Stopped test after 65 mm deflection) | LNL-1- Shear failure

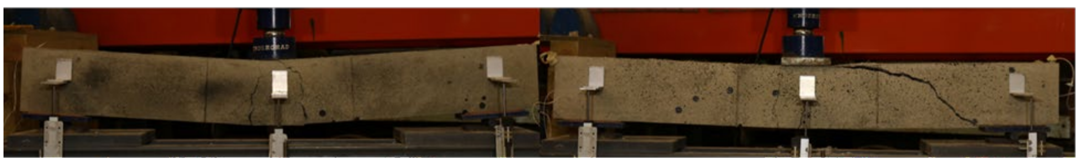

NSC-1- Concrete crushing | LHL-1- Shear failure

HFC-1- Combined flexural/shear failure | NHN-1- Concrete crushing

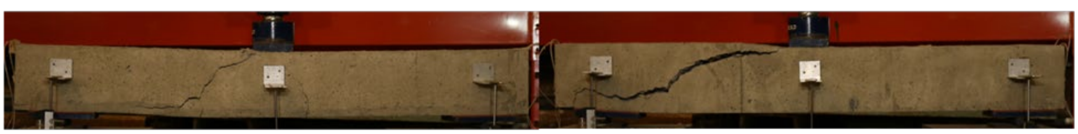

H20-1- Shear/bond failure | LNL-2- Shear failure

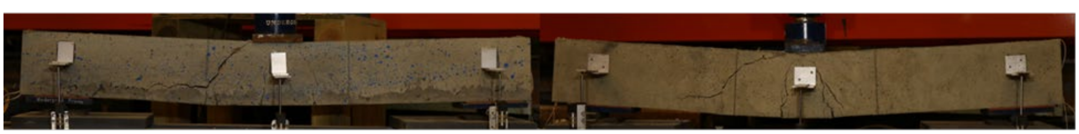

H35-1- Shear/bond failure | NHN-2- Shear failure

H35-2- Shear/bond failure | H50-1-Concrete Crushing

Figure 6. Beam specimens after failure

4.2 Longitudinal Reinforcement Strain Measurements

Figure 7 shows the strain along the length of reinforcement for each of the specimens at 12.5 kN, which, at approximately half the beam capacity, represented a typical service load. The vertical lines above the plots represent the location of cracks on the bottom surface of the beams, where the line type on the crack plot corresponds to the line type on the strain plot. The data is displayed for the 1 m tested span from support to support. To account for the effects of local bending of the bar, both sides of the rebar were instrumented with FOS, and then these measurements were averaged (as recommended by Davis et al. [8]). However, in the case of NHN-1, one side of the fibre broke and so only one fibre's data was used. The peaks seen in each of the strain plots correspond to the presence of a crack at that location, as the strain in the reinforcement increased across the crack. Typically, the larger the peak, the larger the crack [4]. It also should be noted that due to the small size of the beams tested, there existed different maximum strain values at cracks despite being at the same load in members with the same reinforcement. This can be explained by tension softening effects, which can carry different amounts of tensile stresses directly across narrow cracks [31]. As crack widths vary, the amount of tension stresses carried across each crack varies, leading to inherent variability in smaller specimens that have narrow cracks.

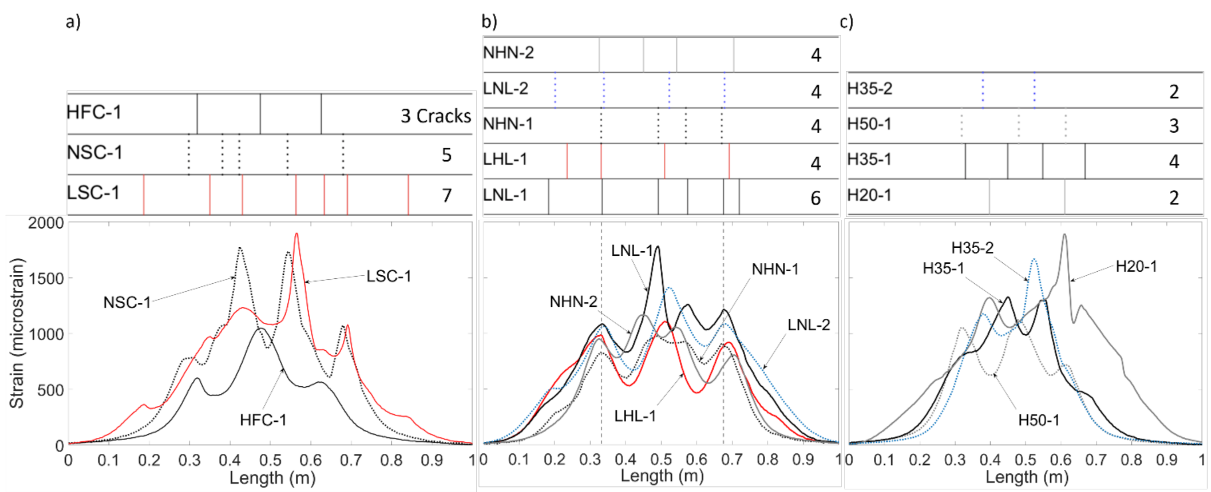

Figure 7. Distributed longitudinal reinforcement strain with crack locations at 12.5 kN load: (a) Control beams, (b)VLFGC beams, (c) HLFGC beams

Figure 7(a) displays the strain behaviour for each of the control specimens, and it can be seen that LSC-1 had the most cracks of the controls and had cracking the closest to the supports. This was expected due to the lower strength of the concrete resulting in a lower cracking moment, leading to more extensive cracking. As seen in both the load deflection and the strain plots, HFC-1 exhibited the highest stiffness, with the lowest strains and smallest number of cracks, which may also be a result of the fibres limiting cracking.

Figure 7(b) presents the reinforcement strains at 12.5 kN for the VLFGC specimens. The concrete interface is represented by the vertical dashed line. A greater number of cracks formed in the VLFGC beams than the HLFGC beams (Figure 7(c)). One or two flexural cracks formed in the centre of the VLFGC beams, but due to the concrete interface and outer regions being composed of normal or low strength concrete, cracks formed at the interface (strain peaks at interface locations) and in the regions closer to the support. The strain measurements at each location in the VLFGC beams, matched the strains in the control beams at that location. For example, for specimen NHN-1, the centre region had HSFRC, and its strains in the centre region were similar to the strains in the centre region of the HFC-1. The strains in the outer region, which consisted of normal strength concrete, were similar to the strains in the outer regions of NSC-1. The same pattern was seen in LHL-1, LNL-1, NHN-2 and LNL-2.

Figure 7(c) illustrates that the presence of a bottom layer of HSFRC limited the number of surface cracks in HLFGC. Both H35-2 and H20-1 had only 2 surface cracks (compared to 5 for the normal strength control), despite having concrete interface problems, such as longitudinal cracking possibly caused by debonding, which will be discussed in later sections. Thus, even a thin layer of HSFRC, such as 20 mm, can limit the number of surface cracks that occur in a beam. However, the strains increased with decreasing thicknesses of HSFRC. H20-1 had the largest maximum strains as well as elevated strains along the entire length. Additionally, strain peaks were seen in locations where surface cracks were not present as will be discussed later. For comparison, the maximum strains for each specimen at 12.5 kN and 21 kN have been provided in Table 4.

Table 4. Maximum strains at 12.5 kN and 21 kN

Specimen	**HFC-1**	**NSC-1**	**LSC-1**	**NHN-1**	**NHN-2**	**LNL-1**
Strain at 12.5 kN (microstrain)	1049	1778	1895	977	1163	1782
Strain at 21 kN (microstrain)	2193	3180	2977	2120	2230	3117
Specimen	**LNL-2**	**LHL-1**	**H20-1**	**H35-1**	**H35-2**	**H50-1**
Strain at 12.5 kN (microstrain)	1412	1107	1892	1329	1666	1122
Strain at 21 kN (microstrain)	-	2367	3359	3090	-	2467

Figure 8 shows the distributed longitudinal reinforcement strains at 21 kN, which is a load just before yield of the longitudinal reinforcement for all the specimens. This load was chosen as FOS strain data is most reliable prior to yielding using this combination of fibre and coating, as also noted by Brault and Hoult [4]. Figure 8(a) shows the reinforcement strain for each of the three controls at 21 kN. Similar behaviour can be seen at 21 kN that was seen at 12.5 kN, with the largest number of cracks (8) in LSC-1, followed by NSC-1 (7) and HFC-1 (5). Also, strains and cracking in outer regions continue to increase with decreased concrete strength. Figure 8(b) displays the reinforcement strain of the VLFGC beams at 21 kN. Since LNL-2 did not reach 21 kN, it was not included in this figure. As seen with the 12.5 kN FOS strain data, more cracks existed in the VLFGC beams than the HLFGC beams. Also as mentioned with the 12.5 kN data, each region of the VLFGC beams had strains that were similar to the control beams that had the same type of concrete.

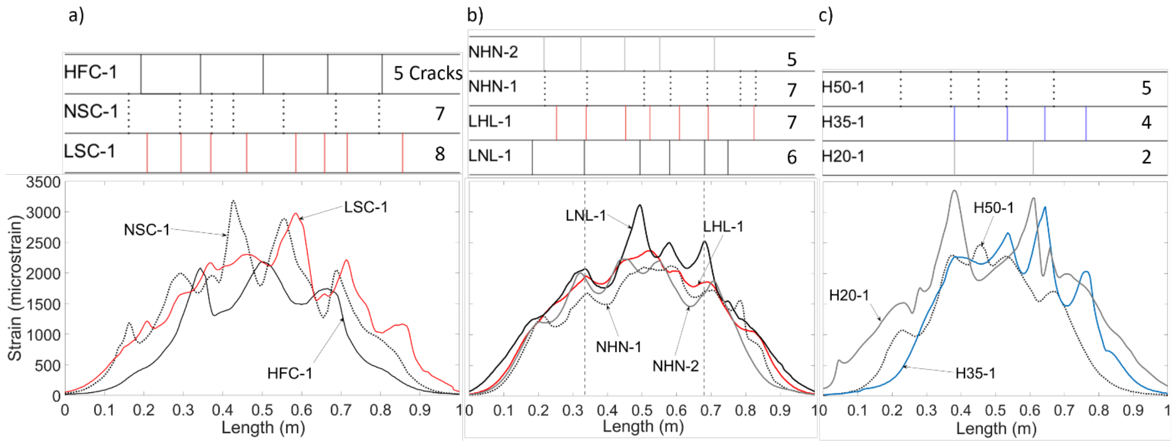

Figure 8. Distributed longitudinal reinforcement strain with crack locations at 21 kN load: (a) Control beams, (b)VLFGC beams, (c) HLFGC beams

Figure 8(c) shows the longitudinal reinforcement strain of the HLFGC beams at 21 kN. H35-2 did not reach 21 kN, so it was not included in this figure. The number of cracks continued to be limited by the presence of HSFRC. The amount of surface cracks in all HLFGC beams was less than or equal to the number of cracks found in the HSFRC control. Similar to 12.5 kN, the strain behaviour of the rebar correlated to the amount of HSFRC in the beam. In the H35-1 specimen, there were small strains on the left side of the beam (0-0.3 m) and larger strains on the right side of the beam (0.8-1 m). From about 0.1 m to about 0.3 m, a horizontal crack formed at the reinforcement level, which was the interface level, at failure. This weak plane prevented vertical cracks from forming across the reinforcement and creating strain peaks. This may have caused more cracking on the right side of the beam as a result. However, H20-1 had elevated strains along the entire length of the beam.

Figure 9(a) shows the distributed reinforcement strains from one of the two fibres (channel 1) on the rebar of H20-1. From the 12.6 kN load to the drop in load to 10.8 kN 0.5 seconds later, the strains not only saw a spike at a single point (0.4 m), but also a uniform increase in strain along the entire length of the left side of the beam. The strain peak at 0.4 m was the formation of surface flexural crack. However, strains on the left side of the beam increased significantly from 10.8 kN to 17.4 kN. Additionally, a few strain peaks were seen on the left side of the beam, even though no surface cracks were seen or detected with DIC at these locations at these loads. Additionally, as seen in Figures 7(c) and 8(c), strains on both sides of the beams were much higher than other specimens.

In order to investigate this behaviour, concrete around the reinforcement in H20-1 was chipped away. Figure 9(b) shows the exposed rebar after chipping. The surface shown in the image is the face of the flexural crack that formed at 0.4 m in Figure 9(a). Two cracks were found to have formed around the reinforcement in a nearly horizontal plane. These cracks may be evidence of the loss of bond between the concrete and the reinforcement resulting in the higher than expected longitudinal strains seen in Figure 9(a). It also should be noted that one of the cracks propagated along the concrete interface. The concrete was also chipped away on the other side of the beam at the face of the flexural crack at 0.6 m in Figure 9(a) and similar cracks were also noted on this face as well. From this investigation, it is most likely that longitudinal splitting cracking occurred internally in this beam during loading. The beam eventually failed in shear, with the longitudinal crack propagating along the concrete interface. The presence of the longitudinal cracking at smaller loads may have created a weak plane for the shear crack to form along. Additionally, it is worth noting that this longitudinal cracking began around service loads and since they were not surface cracks at those loads, they could pose problems that would go unnoticed by visual inspection.

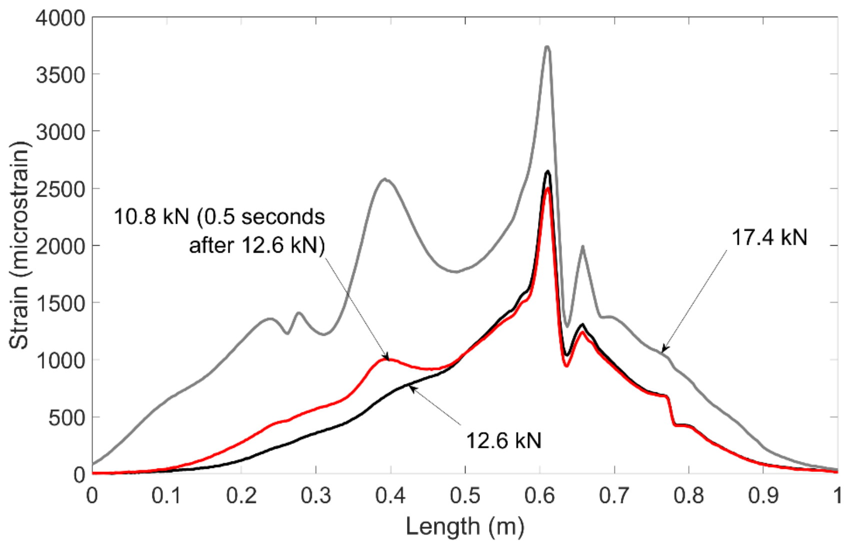

(a) Distributed reinforcement strains before and after longitudinal cracking (channel 1)

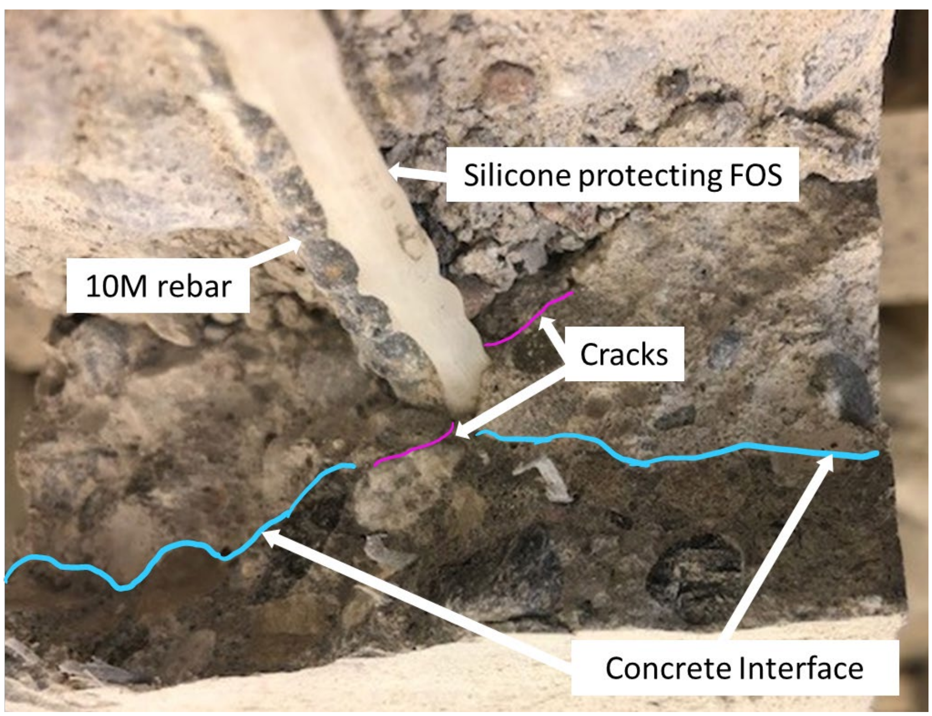

(b) Image of internal cracking

Figure 9. H20-1 longitudinal cracking

Figure 10 shows the distributed reinforcement strains for one of the two fibres installed on the longitudinal reinforcement (Channel 2) of H35-2 at increasing loads. At 14.4kN, typical distributed strain behaviour was seen with low strains in the uncracked regions near supports and two strain peaks at the location of the two flexural surface cracks that formed. However, as load increased to 16.0 kN, a strain peak and strain valley formed next to these flexural cracks towards the supports. This peak and valley then proceeded to move towards the supports as the load was increased to 16.5 kN. This movement of the strain peak coincided with the formation of longitudinal cracking. The left side of the beam formed a horizontal crack at the concrete interface that extended from the flexural crack at 0.4 m to the support as seen in the bottom left of Figure 11(b). Thus, this phenomenon seen in Figure 10 may have been the formation and extension of that crack. Despite this also occurring on the right side of the beam, no surface cracks were seen on that side of the beam. Therefore, as seen with H20-1 and H35-1, H35-2 developed horizontal cracking along the interface that led to the eventual failure mechanism on one side of the beam. Thus, in HLFGC beams with layers at or below the reinforcement level, longitudinal cracking is a potential failure mechanism that, as seen in H20-1 and H35-2, may not appear on the surface. A possible reason for the longitudinal cracking and debonding is differential shrinkage between the two layers. The low strength mix, which had a strength of 16 MPa, and the HSFRC mix, which was more than three times stronger, would experience different amounts of shrinkage. This shrinkage difference may contribute to the development of strains and potentially even microcracking at the interface creating a plane of weakness. Once load is applied, this plane of weakness may have resulted in longitudinal cracking and debonding.

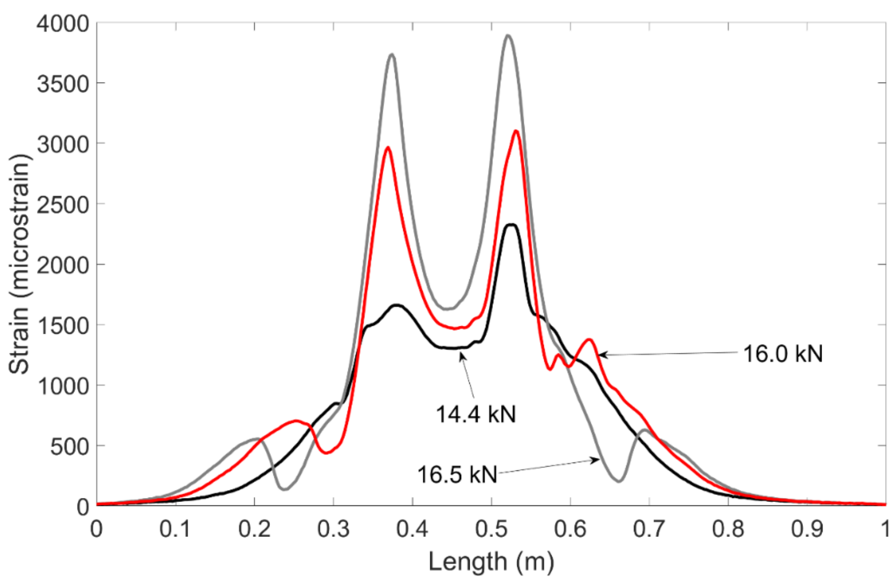

Figure 10. H35-2 distributed longitudinal strains from one fibre (Channel 2)

4.3 Crack Patterns and Widths

Figure 11 displays the crack patterns measured using DIC for each of the beams at 12.5 kN and 21 kN. The dashed lines on the beams, represent the vertical concrete interfaces. At the bottom left of Figure 11(a), the maximum crack widths of the largest crack in each beam at the reinforcement level at 12.5 kN is given. The largest cracks occurred in specimens H20-1 and H35-2, while the smallest maximum crack width was measured on NHN-2. The cracks that had the maximum widths are bolded in red on the crack pattern images in Figure 11(a). At the left in Figure 11(a), the control beam crack patterns are shown. The crack pattern results measured using DIC matched the FOS results in terms of number of cracks and crack spacing. Figure 11(b) shows the crack patterns at 21 kN, a load just prior to yielding. Beams LNL-2 and H35-2 both failed at loads below 21 kN, so crack patterns are provided at loads of 0.5 kN before failure. Generally, existing cracks lengthened and began to turn towards the centre of the beam as flexural cracks turned into shear cracks. Additionally, most beams saw an increase in the number of cracks as the load increased. The H20-1 crack patterns showed the beginnings of the longitudinal cracking at the left side of the beam, while the crack on H35-2 had propagated horizontally by 17.5 kN.

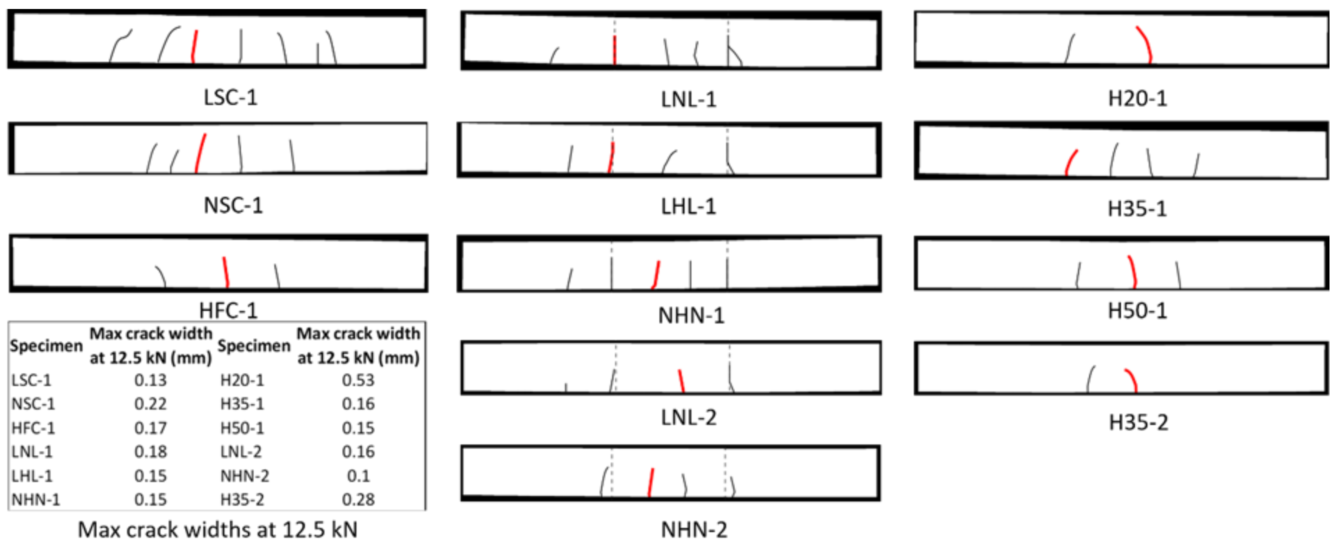

Specimen	Max crack width at 12.5 kN (mm)	Specimen	Max crack width at 12.5 kN (mm)
LSC-1	0.13	H20-1	0.53
NSC-1	0.22	H35-1	0.16
HFC-1	0.17	H50-1	0.15
LNL-1	0.18	LNL-2	0.16
LHL-1	0.15	NHN-2	0.1
NHN-1	0.15	H35-2	0.28

(a) at 12.5 kN load

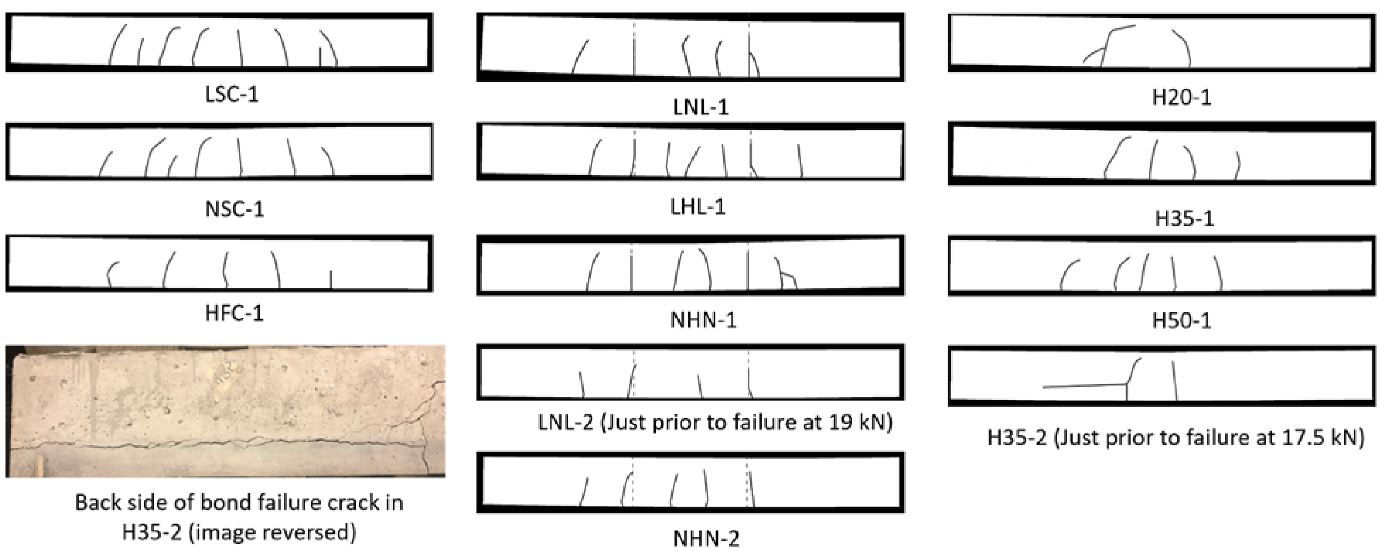

(b) at 21 kN load

Figure 11. Crack patterns based on DIC measurements

Figure 12 shows the critical crack widths versus load measured using DIC at the reinforcement level for each of the FGC specimens. The critical crack width was defined as the largest crack width at a load of 12.5 kN, which was taken as the service load. These values were compared to a 0.18 mm crack width, which is the crack width limit for concrete exposed to deicing chemicals according to the American Concrete Institute (ACI) document ACI 224R-01(08) [32]. Comparing the crack widths, the first thing that was apparent is the variability in widths, which is partially due to different concrete types and the use of FGC but also may be a result of the specimen size [31]. However, observations can be made about some general trends and outliers. First of all, H35-2 and especially H20-1 saw steep increases in crack widths right after crack formation and saw widths higher than the rest of the specimens. These two specimens also developed longitudinal cracks that led to bond failures, indicating that the plane of weakness at the horizontal interface could result in large increases in flexural crack widths at lower loads, before these horizontal cracks appear on the surface of the beam. In addition to ultimate limit state concerns associated with debonding, this may also bring about some serviceability concerns for HLFGC beams with layers at or below the reinforcement level in addition to the previously highlighted impact on capacity. To a lesser extent, this was also seen with H35-1, which also developed horizontal cracking. Aside from those HLFGC specimens, the crack widths for the other FGC specimens mostly remained below those of the normal strength control, NSC-1, indicating that generally crack widths were not an issue with VLFGC specimens and HLFGC specimens with the interface above the reinforcement. On the whole, limited trends could be discerned from the FGC specimens, but the crack widths do increase linearly at approximately the same slope for the FGC specimens, indicating reinforcement had an effect on these crack widths. However, VLFGC beams with HF concrete in the middle did tend to have lower slopes, showing the increased stiffness in the region where flexural cracking occurs due to increased concrete strength and fibres bridging cracks.

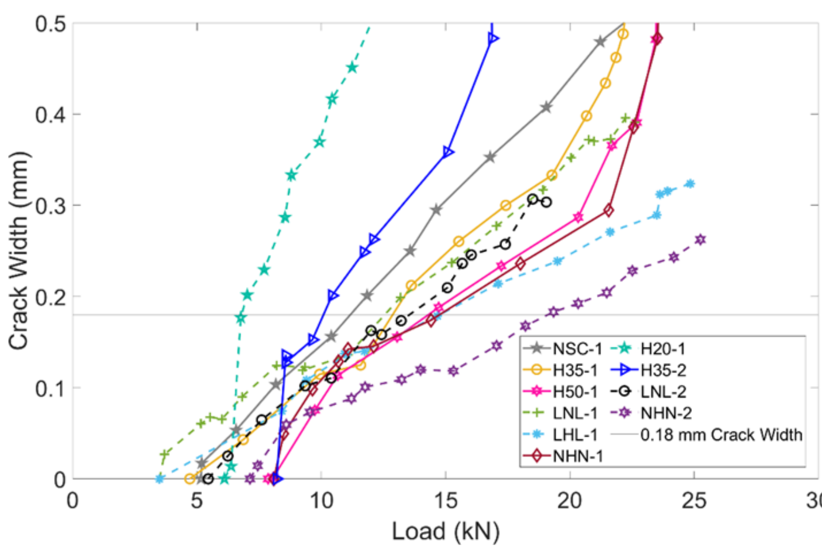

Figure 12. Crack widths measured using DIC for Normal Control and FGC beams

4.4 Behaviour at Vertical Interfaces

Figure 13 presents the concrete cracking stresses in the uniform and VLFGC beams. Each cluster of bars in the figure represents a different type of concrete with HF being the high strength fibre reinforced concrete, NS being the normal strength concrete, LS being the low strength concrete, LS-HF being the interface between LS and HF, LS-NS being the interface between LS and NS, and NS-HF being the interface between NS and HF. The stress at each crack was calculated by first determining the load at which the crack formed using the distributed dynamic FOS strain data (i.e. the load at which a strain peak began to appear). The moment could then be calculated based on the load and the location of the crack along the beam. The stress was then calculated using beam theory. It should be noted that only cracks that developed where the plane sections remain plane corollary of a linear stress profile assumption was valid were included in Figure 13. For example, two cracks that formed in LHL-1 in the centre region at 17.3 kN (9.5 MPa) and 20.0 kN (9.8 MPa) were not included as the extensive cracking of the beam meant that the stress profile could no longer reasonably be taken as linear. From Figure 13, it can be seen that the non-interface cracks had cracking stresses that were consistent with Canadian concrete design code [33] predictions, as the averages of these cracking stresses for each concrete were within 0.5 MPa of the predicted stress. Furthermore, it can be seen that whether the crack formed in a uniform beam or a VLFGC beam as well as whether the crack formed in a centre region of a VLFGC beam or an outer region of a VLFGC beam made little to no difference on the cracking stress. The statistical analysis can be seen in Table 5. Each of the non-interface concrete cracking stress types had coefficients of variation at or below 16%, and coefficients of variation around 15% are reasonably low for cracking values of small specimens [34].

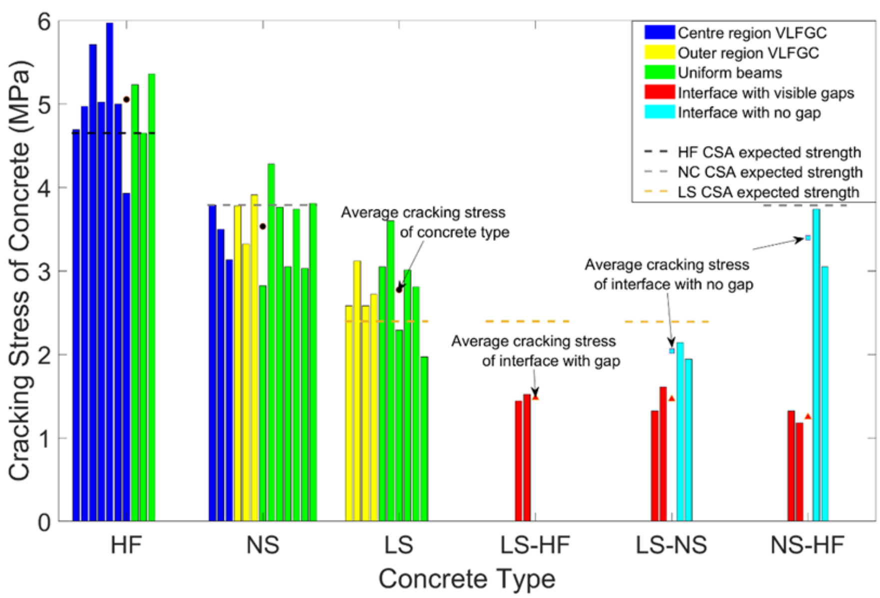

Figure 13. Cracking stresses of concrete in beam specimens

Table 5. Statistical analysis of cracking stresses in concrete (not including interfaces)

	Average (MPa)	St. Dv. (MPa)	COV	Min (MPa)	Max (MPa)
HF	5.05	0.54	11%	3.93	5.97
NS	3.53	0.41	12%	2.82	4.28
LS	2.77	0.44	16%	1.97	3.60

On the other hand, the interface cracking stresses were generally lower than the expected cracking stresses. The VLFGC interfaces that were a part of the first group of beams, had generally larger visible gaps at the interface than the second group of VLFGC beams. The predicted stresses for the interface cracks were assumed to be the cracking stress of the lower strength concrete of the two concretes on either side of the interface. For the interfaces with visible gaps, the average cracking stress only reached 62%, 61%, and 33% of the predicted stress for interfaces LS-HF, LS-NS, and NS-HF, respectively. However, for the interfaces with no visible gaps, the average cracking stress reached 85% and 90% of the predicted cracking stress for interfaces LS-NS and NS-HS. The fact that one specimen only reached a third of the predicted cracking stress indicates the need for better understanding of behaviour of fresh on fresh cast concrete interfaces. These interfaces cracked at loads lower than ordinary concrete, especially when the bond between the two layers was not adequate. This early cracking may be a result of the gap lowering the beam cross sectional area at the interface. Nevertheless, the increase in strength, seen with the better concrete interfaces as a result of better vibration and workability, displayed the possibility of having vertical interfaces that crack at loads that are similar to the cracking loads of ordinary concrete.

Figure 14 shows the progression of the longitudinal reinforcement strains in the VLFGC beams from 5 kN to 12.5 kN to 21 kN and the differences between the original specimens that had visible gaps and the redone specimens with no visible gaps. The interface in Figure 14 is marked by a vertical dashed line on either side of the beam. Figure 14(a) shows the progression of the LNL specimens although it should be noted that LNL-2 at 21 kN was not included as the beam failed before this load. For both LNL-1 and LNL-2, the first cracks to form were the interface cracks. Additionally, strains at these interfaces were similar between LNL-1 and LNL-2 at both 5 and 12.5 kN. Thus, at low loads, the improved interface bond did little to improve the strain behaviour. Additionally, at 12.5 kN and beyond, the maximum strains in the reinforcement were not at the interface. Instead, the maximum strains were seen at midspan of the beams, as is the case in ordinary RC beams. Thus, stress concentrations at these vertical interfaces do not seem to be the location of maximum stress in the beam. Figure 14(b) shows the strain distribution changes with load for the NHN specimens. Limited differences were seen between NHN-1 and NHN-2 in strains at loads of 12.5 kN and higher. Maximum strains were again at midspan instead of at the interfaces. However, while NHN-1 had interface cracking at 5 kN, NHN-2 did not. In fact, the first crack to form in NHN-2 was a midspan flexural crack although the interfaces did crack shortly after the formation of the first flexural crack. Nevertheless, cracking of the interface at higher loads than typical midspan flexural cracking loads was achieved with better construction of the beams.

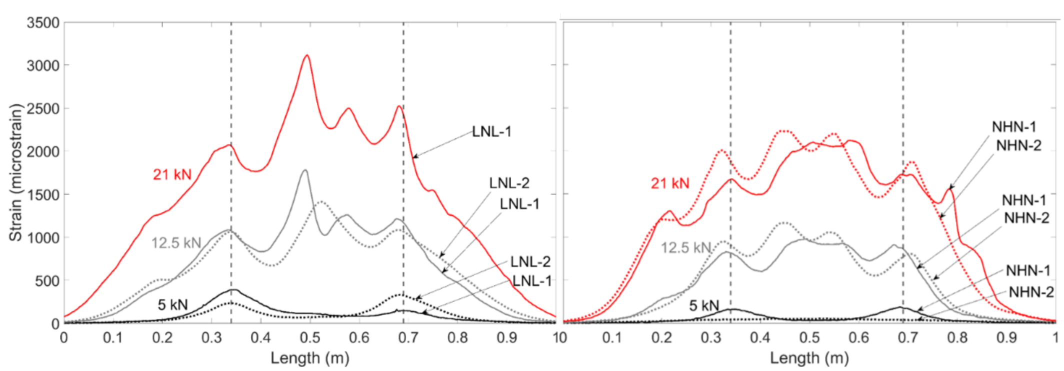

(a) LNL (b) NHN

Figure 14. Progression of distributed longitudinal strain measurements including impact of interface between sections

5. Discussion

Overall, large variability existed in the load deflection behaviour of FGC. When constructed with a minimal gap at the interface, VLFGC specimens with HSFRC can have higher load carrying capacity, ductility, stiffness, and cracking load than a uniform normal concrete beam as noted in previous research with FGC and FRC [13-18]. HLFGC resulted in load carrying capacities similar to the normal strength control but contributed to a higher cracking load. Despite these potential benefits of using FGC, brittle failures, such as shear and bond failures (also seen by [15]), at loads less than the controls demonstrated the need for more investigation into the behaviour of FGC with larger specimens. FGC strain behaviour varied with concrete type for VLFGC specimens and depended on the layer thickness for HLFGC. However, concrete interfaces for both types of FGC resulted in elevated strains at interfaces for VLFGC and at interfaces at or below reinforcement levels for HLFGC. HLFGC beams tended to have lower numbers of surface cracks than NSC-1 and VLFGC beams as a result of the bottom layer that contained PP fibres, while VLFGC specimens had similar numbers of cracks as NSC-1. Crack widths tended be larger at earlier loads for HLFGC beams with interface bond issues such as gaps, while cracks grew more slowly for VLFGC beams with a centre region of HF concrete. Cracks also preferentially formed at early loads at vertical interfaces with visible gaps. However, at interfaces without visible gaps, interface cracking was delayed and expected cracking stresses according to CSA A23.3 were nearly achieved. Limited research exists on functionally graded reinforced concrete and less so on distributed fibre optic strain sensors and DIC on FGC. Thus, the evaluation of results in the context of current research was limited. The future use numerical modelling and nonlinear finite element analysis with FGC may help evaluate results seen in this experimental program.

6. Conclusions

This experimental campaign investigated the performance of functionally graded concrete (FGC) by testing 9 different types of specimens (three types of control, three types of vertically layered FGC (VLFGC), and three types of horizontally layered FGC (HLFGC) beams). The beams were tested in three point bending to failure, they were instrumented with displacement transducers and distributed fibre optic strain sensors on the longitudinal reinforcement, and digital image correlation was used to measure surface cracking. The following are the key findings from the campaign:

1. The presence of a horizontal layer of high strength fibre reinforced concrete (HSFRC) did not increase the load carrying capacity compared to a uniform normal strength concrete beam but it did increase the cracking load. However, horizontal layers at or below reinforcement level led to longitudinal cracking, possibly due to differential shrinkage, which led to debonding and brittle failures.
2. A vertical layer of high strength fibre reinforced concrete in the centre region increased the load carrying capacity but did not increase the cracking load due to the formation of cracks at the interface between concrete types. Additionally, outer regions of low strength concrete often led to brittle shear failures.
3. Strains along the length of reinforcement in FGC were measured and were used to identify cracks as local strain peaks. The strains in HLFGC beams decreased as the thickness of the high strength concrete layer increased. However, longitudinal cracking in HLFGC beams with layers at or below the reinforcement level led to increases in strains due to the internal longitudinal cracking that was captured by the FOS strain data but not on the surface of the beam.

4. VLFGC reinforcement strain patterns and magnitudes depended on the concrete type at each location and the presence of the concrete interfaces, as cracking was found to occur at the interfaces from FOS strain data. These interface cracks were, for the most part, the first cracks to form. However, when a fully bonded interface was achieved in one case, the first crack instead occurred at midspan. Interface cracking in this case occurred at higher loads than the other VLFGC beams, closer to the expected cracking loads of ordinary concrete.
5. The location of cracks measured with FOS were confirmed by DIC, in addition to measuring crack widths and capturing their development beyond the level of the reinforcement and in the longitudinal direction. Crack widths in the HLFGC beams with layers at or below the reinforcement level were larger than in the other beams tested.
6. Cracking stresses at the vertical interfaces can be as low as a third of the Canadian concrete code predicted cracking stress, but with a fully bonded interface, the cracking stress was as much as 90% of the code predicted cracking stress.

Acknowledgements

This work was supported by the Natural Sciences and Engineering Research Council of Canada, Government of Ontario, and Transport Canada. The authors also would like to thank Chris Christidis from Sika Group for providing fibres and superplasticizer. Finally, the authors thank Andre Brault, Julia Coghlan, Janet Lees, Serena Li, Branna MacDougall, Demewoz Menna, Jack Poldon, and Paul Thrasher for their help with this research.

References

[1] Van Den Heede, P., & Belie, N. D. (2012). Environmental impact and life cycle assessment (LCA) of traditional and ‘green’ concretes: Literature review and theoretical calculations. *Cement and Concrete Composites, 34*(4), 431-442. doi:10.1016/j.cemconcomp.2012.01.004

[2] Low, M. (2005). *Material flow analysis of concrete in the United States* (Unpublished doctoral dissertation). Massachusetts Institute of Technology.

[3] Torelli, G., Fernández, M. G., & Lees, J. M. (2020). Functionally graded concrete: Design objectives, production techniques and analysis methods for layered and continuously graded elements. *Construction and Building Materials, 242*, 118040. doi:10.1016/j.conbuildmat.2020.118040

[4] Brault, A., & Hoult, N. (2019). Distributed Reinforcement Strains: Measurement and Application. *ACI Structural Journal, 116*(4), 115-127. doi:10.14359/51714483

[5] Fayyad, T. M., & Lees, J. M. (2014). Application of Digital Image Correlation to Reinforced Concrete Fracture. *Procedia Materials Science, 3*, 1585-1590. doi:10.1016/j.mspro.2014.06.256

[6] Hoult, N. A., Dutton, M., Hoag, A., & Take, W. A. (2016). Measuring Crack Movement in Reinforced Concrete Using Digital Image Correlation: Overview and Application to Shear Slip Measurements. *Proceedings of the IEEE, 104*(8), 1561-1574. doi:10.1109/jproc.2016.2535157

[7] Regier, R., & Hoult, N. A. (2015). Concrete deterioration detection using distributed sensors. *Proceedings of the Institution of Civil Engineers - Structures and Buildings, 168*(2), 118-126. doi:10.1680/stbu.13.00070

[8] Davis, M. B., Hoult, N. A., Bajaj, S., & Bentz, E. C. (2017). Distributed Sensing for Shrinkage and Tension Stiffening Measurement. *ACI Structural Journal, 114*(3), 753-764. doi:10.14359/51689463

[9] Barrias, A., Casas, J., & Villalba, S. (2018). Embedded Distributed Optical Fiber Sensors in Reinforced Concrete Structures—A Case Study. *Sensors, 18*(4), 980-1001. doi:10.3390/s18040980

[10] Poldon, J. J., Hoult, N. A., & Bentz, E. C. (2019). Distributed Sensing in Large Reinforced Concrete Shear Test. *ACI Structural Journal*, *116*(5), 235-245. doi: 10.14359/51716765

[11] Maalej, M., & Li, V. (1995). Introduction of Strain-Hardening Engineered Cementitious Composites in Design of Reinforced Concrete Flexural Members for Improved Durability. *ACI Structural Journal, 92*(2), 167-176. doi:10.14359/1150

[12] Maalej, M., Ahmed, S. F., & Paramasivam, P. (2003). Corrosion Durability and Structural Response of Functionally-Graded Concrete Beams. *Journal of Advanced Concrete Technology, 1*(3), 307-316. doi:10.3151/jact.1.307

[13] Roesler, J., Paulino, G., Gaedicke, C., Bordelon, A., & Park, K. (2007). Fracture Behavior of Functionally Graded Concrete Materials for Rigid Pavements. *Transportation Research Record: Journal of the Transportation Research Board, 2037*(1), 40-49. doi:10.3141/2037-04

[14] Evangelista, F., Roesler, J., & Paulino, G. (2009). Numerical Simulations of Fracture Resistance of Functionally Graded Concrete Materials. *Transportation Research Record: Journal of the Transportation Research Board, 2113*(1), 122-131. doi:10.3141/2113-15

[15] Li, Q., & Xu, S. (2009). Experimental investigation and analysis on flexural performance of functionally graded composite beam crack-controlled by ultrahigh toughness cementitious composites. *Science in China Series E: Technological Sciences, 52*(6), 1648-1664. doi:10.1007/s11431-009-0161-x

[16] Naghibdehi, M. G., Mastali, M., Sharbatdar, M. K., & Naghibdehi, M. G. (2014). Flexural performance of functionally graded RC cross-section with steel and PP fibres. *Magazine of Concrete Research, 66*(5), 219-233. doi:10.1680/macr.13.00248

[17] Li, P., Sluijsmans, M., Brouwers, H., & Yu, Q. (2020). Functionally graded ultra-high performance cementitious composite with enhanced impact properties. *Composites Part B: Engineering, 183*, 107680. doi:10.1016/j.compositesb.2019.107680

[18] Moghadam, A. S., & Omidinasab, F. (2020). Assessment of hybrid FRSC cementitious composite with emphasis on flexural performance of functionally graded slabs. *Construction and Building Materials, 250*, 118904. doi:10.1016/j.conbuildmat.2020.118904

[19] Collins, M. P., & Kuchma, D. (1999). How safe are our large, lightly reinforced concrete beams, slabs, and footings?. *Structural Journal*, *96*(4), 482-490.

[20] Herrmann, M., & Sobek, W. (2016). Functionally graded concrete: Numerical design methods and experimental tests of mass-optimized structural components. *Structural Concrete, 18*(1), 54-66. doi:10.1002/suco.201600011

[21] Nes, L. G., & Øverli, J. A. (2015). Structural behaviour of layered beams with fibre-reinforced LWAC and normal density concrete. *Materials and Structures, 49*(1-2), 689-703. doi:10.1617/s11527-015-0530-9

[22] Liu, X., Yan, M., Galobardes, I., & Sikora, K. (2018). Assessing the potential of functionally graded concrete using fibre reinforced and recycled aggregate concrete. *Construction and Building Materials, 171*, 793-801. doi:10.1016/j.conbuildmat.2018.03.202

[23] Torelli, G., & Lees, J. M. (2020). Interface bond strength of lightweight low-cement functionally layered concrete elements. *Construction and Building Materials, 249*, 118614. doi:10.1016/j.conbuildmat.2020.118614

[24] Bajaj, K., Shrivastava, Y., & Dhoke, P. (2013). Experimental Study of Functionally Graded Beam with Fly Ash. *Journal of The Institution of Engineers (India): Series A, 94*(4), 219-227. doi:10.1007/s40030-014-0057-z

[25] Chan, R., Liu, X., & Galobardes, I. (2020). Parametric study of functionally graded concretes incorporating steel fibres and recycled aggregates. *Construction and Building Materials, 242*, 118186. doi:10.1016/j.conbuildmat.2020.118186

[26] Heinz, P., Herrmann, M., & Sobek, W. (2012). *Production Method and Application of Functionally Graded Components in Construction (Herstellungsverfahren und Anwendungsbereiche für funktional gradierte Bauteile im Bauwesen)*. Stuttgart: Fraunhofer IRB Verlag.

[27] Canadian Standards Association. (2019). Carbon Steel Bars for Concrete Reinforcement (CSA G30.18-09). *CSA Group, Mississauga, ON, Canada*.

[28] Sika Group. (2020). *SikaFiber Force 600 Product Data Sheet*. Pointe-Claire, QC.

[29] Luna Technologies. (2020). *Luna ODiSI 6000 Data Sheet*. Blacksburg, VA.

[30] Vecchio, F. J., & Collins, M. P. (1986). The Modified Compression-Field Theory for Reinforced Concrete Elements Subjected to Shear. *ACI Journal Proceedings, 83*(2), 219-231. doi:10.14359/10416

[31] Cornelissen, H., Hordijk, D., & Reinhardt, H. (1986). Experimental determination of crack softening characteristics of normalweight and lightweight. *Heron*, *31*(2), 45-46.

[32] ACI Committee 224. (2008). 224R-01(08): Control of Cracking in Concrete Structures. doi:10.14359/10632

[33] Canadian Standards Association. (2014). Design of Concrete Structures (CSA A23. 3-14). *CSA Group, Mississauga, ON, Canada*.

[34] Bentz, E. C., Vecchio, F. J., & Collins, M. P. (2006). Simplified modified compression field theory for calculating shear strength of reinforced concrete elements. *ACI Structural Journal*, *103*(4), 614.